

DETAILED COMPARISON OF THE PERFORMANCE BETWEEN A SIMPLE AND A MODIFIED MONO-BLOCK-LAYER-BUILT TYPE SOLID OXIDE FUEL CELL

by

**Jose J. RAMIREZ-MINGUELA^{a*}, Jorge A. ALFARO-AYALA^a,
Agustin R. URIBE-RAMIREZ^a, Jesus I. MINCHACA-MOJICA^a,
Beatriz RUIZ-CAMACHO^a, Juan M. MENDOZA-MIRANDA^b,
and Carlos E. ALVARADO-RODRIGUEZ^a**

^a Department of Chemical Engineering, University of Guanajuato, DCNE,
Guanajuato, Gto., Mexico

^b Unidad Profesional Interdisciplinaria de Ingenieria Campus Guanajuato,
Instituto Politecnico Nacional, Silao de la Victoria, Gto., Mexico

Original scientific paper

<https://doi.org/10.2298/TSCI201131170R>

A detailed comparison of the performance between a simple mono-block-layer-build type solid oxide fuel cell geometry and a mono-block-layer-build type solid oxide fuel cell with an embedded porous pipe in the air supply channel is carried out. The study considers constant and variable porosities along the porous pipe, fed with an air-flow in a counter-flow arrangement. Four cases are analyzed: without the porous pipe, with a pipe of constant porosity, with two different porosities, and with four variable porosities. This work is based in a 3-D CFD model that considers the phenomena of mass transfer, heat transfer, species transport, and electrochemical reactions. Detailed comparisons of the voltage, temperature, and species concentration are illustrated. The electrode-electrolyte interface contours of species concentration, temperature, and electric fields are compared. The results show that there is approximately twice the current density in the geometry that considers the two different porosities compared to the simple geometry. The consumption of hydrogen has the same behavior for the entire tested current density, while the availability of oxygen at the cathode-electrolyte interface is improved in cases with porous pipe compared to the simple mono-block-layer-build type geometry. The use of a porous pipe embedded in the air channel showed that it is possible to have a wider operating range of a mono-block-layer-build type solid oxide fuel cell, and allowed to obtain a more homogeneous temperature distribution on the electrode-electrolyte interface of the solid oxide fuel cell, consequently, there is the possibility of reducing the thermal stress in the solid oxide fuel cell.

Key words: *solid oxide fuel cell, CFD, mono-block-layer-build type geometry, porous pipe*

Introduction

In the past decades, solid oxide fuel cells (SOFC) have emerged as an alternative to the conventional electricity generation systems for residential and power plants due to their higher energy conversion efficiencies and power densities, lower production costs, lower en-

* Corresponding author, e-mail: jjd.ramirezminguela@ugto.mx

vironmental impact, and the capability of being coupled with power plant applications [1-3]. SOFC is one of the promising types of the fuel cell that generally operates at high temperatures ranging from 873-1273 K [4-6]. There are many different kinds of SOFC, according to the configuration, which can be divided into planar type SOFC, tubular type SOFC, mono-block-layer-built (MOLB) type SOFC, the segmented-in-plane type SOFC and so on [7-9]. The advantage of a planar SOFC is its low electrical resistance, its simplicity in fabrication, low cost, easy assembly of stack, and high efficiency. Its disadvantage is that it presents difficult sealing given differences in the thermal expansion coefficients of ceramic cells and metal materials at high temperature during stacking [10-12]. The main advantage of tubular SOFC is the simplified sealing technology, simple cell assembly and strong anti-stress ability, however, the low power density and high cost of the tubular SOFC restrict its commercial development. Compared with other SOFC, the MOLB type SOFC not only increases the reaction area, but also provides gas channel, which reduces the thickness and weight of the interconnector and improves the power density per volume or weight [13, 14]. The MOLB type SOFC geometry design improves the mechanical strength and the cell stacks are more compact. Investigations of planar and MOLB type SOFC, about operation and performance, have predicted the temperature distributions for various flow rates. Thinh [15] developed a 3-D model for transient performance of a SOFC which showed higher temperature gradients along the cell at different time steps. Amiri *et al.* [16] modeled a SOFC system, fuel cell stack with its auxiliary components. Their results showed higher temperature gradients inside the fuel cell. Chelmehsara and Javad [17] compared different types of self-supported SOFC. They reported the temperature distributions inside the cell with high temperature gradients. Hwang *et al.* [18] obtained results about the local transport characteristics inside the MOLB type SOFC, such as: the reactant gas concentration distribution, the overpotential distribution, and the current density distribution. Yunzhen *et al.* [19] compared the temperature distribution of planar and MOLB type SOFC obtaining higher temperature gradients.

Moreover, Ramirez-Minguela *et al.* [20] investigated how the operating conditions and the electrolyte thicknesses affect the prediction of the thermodynamic irreversibility by means of an entropy generation analysis of a MOLB type SOFC. They reported the temperature distributions inside the cell with high temperature gradients. Ramirez-Minguela *et al.* [21] studied a MOLB type SOFC by means of an energy and entropy analysis using biogas for four different biogas compositions. They reported the temperature distributions inside the cell with high temperature gradients. Ramirez-Minguela *et al.* [22] evaluated the effect of varying the electrochemical model parameters on the performance and entropy generation of a MOLB type SOFC. They reported the temperature distributions inside the cell with high temperature gradients. Ramirez-Minguela *et al.* [23] analyzed a simple MOLB type geometry. They obtained the performance of the SOFC considering internal reforming of methane in the anode side with different biogas compositions and they proposed a new configuration for the MOLB type geometry that consists of embedding a porous pipe in the air supply channel, which is fed by air through a counter-flow arrangement. The results showed that the biogas from local sludge had the lower temperature gradient and more homogeneous current density distributions along the fuel cell, on the other hand, with the new configuration proposed for the MOLB type geometry the temperature distribution inside of the fuel cell had lower temperature gradients. Ramirez-Minguela *et al.* [24] compared a modified MOLB type SOFC with a porous embedding pipe in the air side of the geometry and a simple planar geometry feeding by biogas from local sludge considering internal reforming of methane in the anode side. They found higher H₂ concentration and lower average temperature value from

the MOLB type with embedding porous pipe geometry, which help to handle higher current densities, to reduce thermal stress and to increase the performance of the fuel cell. It is necessary to highlight that in the previous investigation [23, 24] the authors only considered an average current density of 2000 A/m² for the different cases and they used mainly biogas to feed the SOFC. As it is well known, the higher temperature gradients inside the SOFC are reached when the hydrogen is used as a fuel [20, 22]. In consequence, the thermal stresses are an important issues in the materials of the SOFC.

Therefore, the objective of this study is to complement the analysis made in Ramirez-Minguela *et al.* [23, 24], in a detail way, it means, obtaining the performance of a simple MOLB type geometry and comparing it with a cell that has a porous pipe embedded in the air channel with constant and variable porosity along the porous pipe in the geometry, using hydrogen as fuel and considering different current densities. To achieve this objective, four cases are analyzed:

- without the porous pipe,
- with a pipe of constant porosity,
- with two different porosities, and
- with four variable porosities.

The aim of the porous pipe is to diminish the temperature gradients that are reached at the electrolyte-electrode interface inside the SOFC. The operation of the SOFC is restricted until an average temperature of 1273 K on the interface of the electrode-electrolyte is reached [4-6]. Detailed comparisons of the voltage, temperature, and species concentration are illustrated at different current densities. Finally, the electrode-electrolyte interface contours of species concentration, temperature and electric fields are compared.

Model development

Simple MOLB type SOFC and MOLB type SOFC with a porous pipe embedded in the air channel

A simple MOLB type SOFC, figs. 1(a) and 1(c) is modified with a porous pipe embedded in the air channel, figs. 1(b) and 1(d). The fuel (a mixture of hydrogen and steam) and the air-flow in parallel way into the trapezoidal channels that are separated by the electrodes and the electrolyte (anode-electrolyte-cathode). The porous pipe is fed with a flow of air in a counter-flow arrangement, fig. 1(b). The MOLB unit is symmetric about the mid-planes of the air and the fuel channels. Therefore, the present computational domain considers the region between these two planes for saving computational resources and time. The length of the SOFC is 100 mm.

Mathematical model

In the mathematical model, the following assumptions were considered: steady-state, incompressible Newtonian ideal gas mixture, homogeneous and isotropic porous media, thermal equilibrium between solid, and gas phases.

The oxidation-reduction reaction with hydrogen as fuel was considered, which is expressed:



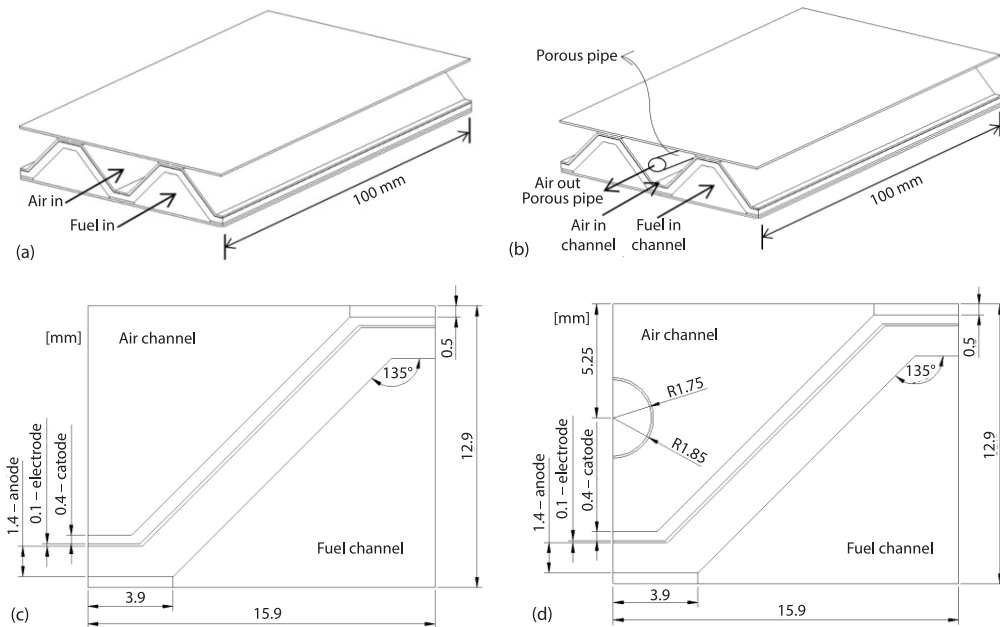


Figure 1. Dimensions of the MOLB type geometry SOFC; (a) without porous pipe, (b) with a porous pipe embedded in the air supply channel, (c) computational domain without porous pipe, and (d) computational domain with a porous pipe embedded in the air supply channel

The continuity and momentum conservation equations:

$$\nabla \rho \vec{v} = 0 \quad (4)$$

$$\rho(\vec{v}\nabla)\vec{v} = -\nabla p + \mu \nabla^2 \vec{v} \quad (5)$$

$$\rho(\vec{v}\nabla)\vec{v} = -\nabla p + \mu \nabla^2 \vec{v} - \frac{\mu}{K} \vec{v} \quad (6)$$

$$\nabla(\rho \omega_i \vec{v}) = -\nabla \vec{J}_i + S_i \quad (7)$$

$$\vec{J}_i = -\rho D_{i,\text{eff}} \nabla \omega_i \quad (8)$$

$$D_{i,\text{eff}} = \frac{\varepsilon}{\tau} D_{ij} \quad (9)$$

$$S_i = \begin{cases} \frac{j}{n_e F} M_i & \text{TPB} \\ 0 & \text{elsewhere} \end{cases} \quad (10)$$

In the porous media, the continuity conservation eq. (4) and the Darcy-Brinkmann eq. (6) are used to model velocity and pressure fields in both anode and cathode. In the fuel and air channels, $D_{i,\text{eff}}$ coincides with D_{ij} , while in the porous media, the effective binary diffusivity is computed by the eq. (9). Electrochemical reactions take place at the three-phase-boundary (TPB),

therefore, the source terms S_i are expressed accordingly to Faraday's law by the eq. (10). The temperature distribution and the heat transfer rate are calculated from the energy conservation equation and its source terms are shown:

$$\nabla \left[\rho \vec{v} \left(h + \frac{v^2}{2} \right) \right] = \nabla \left(k_{\text{eff}} \nabla T - \sum_i h_i \vec{J}_i \right) + S_e \quad (11)$$

$$k_{\text{eff}} = \varepsilon k_g + (1 - \varepsilon) k_s \quad (12)$$

$$S_{e,\text{act}} = j \eta_{\text{act}} \quad (13)$$

$$S_{e,\text{elec}} = \frac{j}{n_e F} T \Delta S \quad (14)$$

$$S_{e,\text{ohm}} = \frac{j^2}{\sigma} \quad (15)$$

$$\sigma_{\text{electrolyte}} = \frac{100}{0.3685 + 0.002838 \exp\left(\frac{10300}{T}\right)} \quad (16)$$

$$\sigma_{\text{cathode}} = \frac{42 \cdot 10^6}{T} \exp\left(-\frac{1200}{T}\right) \quad (17)$$

$$\sigma_{\text{anode}} = \frac{95 \cdot 10^6}{T} \exp\left(-\frac{1150}{T}\right) \quad (18)$$

$$\sigma_{\text{cc}} = \frac{9.3 \cdot 10^6}{T} \exp\left(-\frac{1100}{T}\right) \quad (19)$$

In the porous electrodes, the effective value of the thermal conductivity can be calculated by the eq. (12). The conductivity, the specific heat and the density of the solid material in the different subdomains are outlined in tab. 1.

Table 1. Thermal properties of the solid materials [19]

Properties	Anode	Cathode	Electrolyte
Thermal conductivity [WK ⁻¹ m ⁻¹]	6.23	9.6	2.7
Density [kgm ⁻³]	6200	6000	5560
Specific heat [Jkg ⁻¹ K ⁻¹]	650	900	300

The heat generation due to the activation losses, the electrochemical reactions and the ohmic losses are calculated for the eqs. (13)-(15). The electrical conductivities for the electrolyte, the cathode, the anode and the current collectors are given for the eqs. (16)-(19). The governing equations for the electric field are given:

$$\nabla(\sigma \nabla \phi) = \begin{cases} \frac{-j}{\sigma} & \text{TPB} \\ 0 & \text{elsewhere} \end{cases} \quad (20)$$

$$j = j_0 \left\{ \exp \left[\frac{\beta n_e F}{RT} n_{\text{act}} \right] - \exp \left[- \frac{(1-\beta) n_e F}{RT} n_{\text{act}} \right] \right\} \quad (21)$$

$$V_{\text{rev}} = V^0 + \frac{RT}{2F} \ln \left(\frac{p_{\text{H}_2} \sqrt{p_{\text{O}_2}}}{p_{\text{H}_2\text{O}}} \right) \quad (22)$$

$$V = V_{\text{rev}} - n_{\text{act}} - n_{\text{ohm}} - n_{\text{conc}} \quad (23)$$

Numerical implementation

Model parameters and considerations

The mathematical models for the different MOLB type configurations are solved by coupling the electrochemical reactions with the commercial CFD simulation software (ANSYS-FLUENT®). A computer with 8 Intel® Core™ i7-2670QM cores and 8 GB RAM is used. The Navier-Stokes and the transport equations are solved, with the model parameters given in tab. 2, to obtain the gas species concentrations and temperatures at each cell position.

Table 2. Model parameters of the anode and cathode [19]

Porosity [-]	Tortuosity [-]	Permeability [m ²]	Transfer coefficient [-]
0.3	3	$1.7 \cdot 10^{-10}$	0.5

The numerical information of velocity, temperature and species concentration is linked to the electrochemical model (subroutine). Then, the local current density is calculated and used to obtain the hydrogen reaction rate, the heat source and the species source. The gas species concentration and temperature distributions are then calculated for the next iteration, and so on, until the convergence of the solution is achieved. Scaled residuals are monitored for all the variables and the solution is converged when the residuals are lower than 10^{-6} .

The computational grid has been subsequently refined (from 48000-1500000 cells) and a mesh of 267000 and of 290000 cells has been found to be enough to achieve mesh independent solutions for the cases with and without porous pipe, respectively. The effects in the average current density due to the number of elements used in the mesh is shown in tab. 3 for the porous pipe case. The mesh used for the cases with and without porous pipe can be observed in fig. 2.

Table 3. Mesh sensibility

Number of elements	Average current density [Am ⁻²]	Variation [%]	Convergence time [hour]
37740	8333.57	–	0.4
91200	8551.92	2.55	0.58
135400	8093.25	5.66	0.9
150960	8342.74	3.0	1
189560	8075.46	3.3	1.5
290000	8092.85	0.2	2.3
378800	8081.08	0.15	4
685320	8097.33	0.2	8
812160	8080.56	0.2	9.5
1500000	8095.89	0.18	14

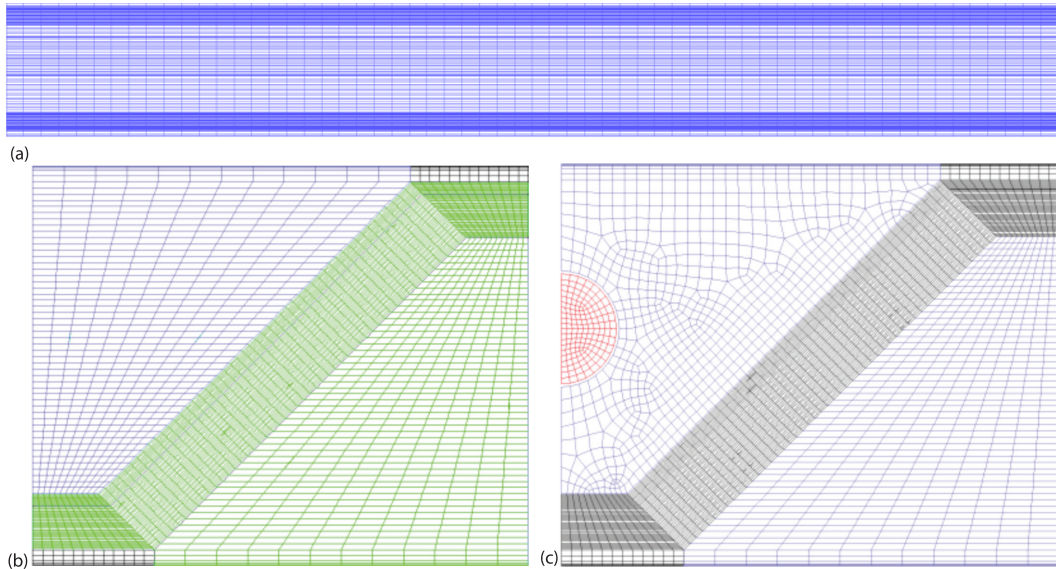


Figure 2. Model meshing: (a) throughout the SOFC for all the cases, (b) computational domain without porous pipe, and (c) computational domain with a porous pipe embedded in the air supply channel

Cases of study and boundary conditions

The analysis of the fuel cell was carried out by considering four cases to compare the effect of the MOLB type geometry on the performance of the SOFC with and without a porous pipe:

- Simple MOLB type geometry without a porous pipe, figs. 1(a) and 1(c).
- The MOLB type geometry with an embedded porous pipe, constant porosity, figs. 1(b), 1(d), and 3(a).
- The MOLB type geometry with an embedded porous pipe with two different porosities, figs. 1(b), 1(d), and 3(b).
- The MOLB type geometry with an embedded porous pipe with four different porosities along the pipe, figs. 1(b), 1(d), and 3(c).

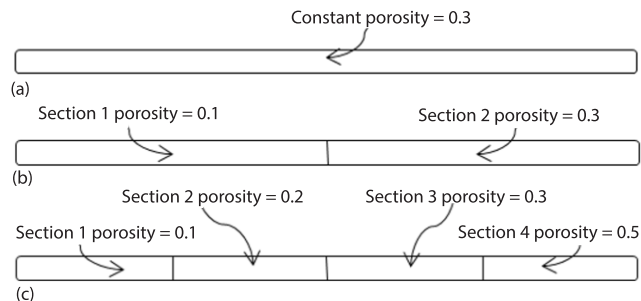


Figure 3. Porous pipe with different porosities for Cases 2-4; (a) constant, (b) 2 sections, and (c) 4 sections

The porous pipe is fed with air in a counter-flow arrangement. In the first case, the air and fuel mass-flows are $9.18 \cdot 10^{-5}$ kg/s and $4.78 \cdot 10^{-6}$ kg/s for the cathode and anode, respectively. The inlet molar fraction of H_2 is 0.49. The fuel and air inlet temperatures are both 1073 K. The ambient pressure is considered at the outlet cross-sections. The fuel cell is considered to be adiabatic and symmetric, the symmetry boundary conditions are imposed on the left and right planes, as shown in fig. 1. The boundary conditions for the MOLB type geometry SOFC with an embedded porous pipe are the same (Cases 2-4), however, the mass-flow of air is $8.66 \cdot 10^{-5}$ kg/s in the cathode side channel, and the mass-flow of air is $1.15 \cdot 10^{-5}$ kg/s in the embedded porous pipe in counter-flow arrangement. The operation of the SOFC is restricted until an average temperature of 1273 K on the interface of the electrode-electrolyte is reached. Finally, the model validation was carried out by comparison of the results with those obtained in [19], observing similar current, species and temperature distributions.

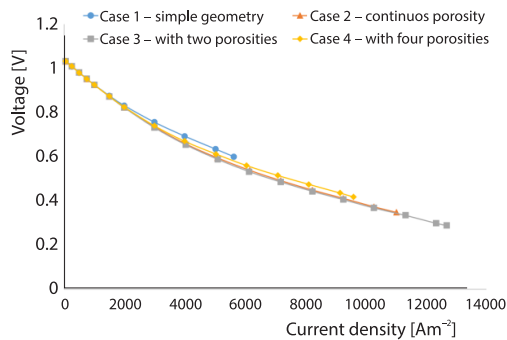


Figure 4. Power density obtained from voltage variation of the cases under study

the embedded porous pipe (Cases 2-4) the maximum current densities obtained are around 11000 A/m², 12700 A/m², and 9600 A/m², which corresponds to a power densities of 3840 W/m², 3660 W/m², and 4000 W/m², respectively.

The average temperature, the minimum temperature gradient, the maximum local temperature and the minimum local temperature of the SOFC are shown in fig. 5 at different current densities.

The temperature of the simple MOLB type geometry increases rapidly as the current density increases in comparison with the cases with the embedded porous pipe. While the current density increases, the average temperature difference increases between the Case 1 and the cases with the embedded porous pipe. In Case 1, for a current density of 5600 A/m², the average temperature is around of 1273 K, while in Cases 2 and 3 for this current density, the average temperature is around of 1140 K, and in Case 4 is around of 1160 K. As it was expected, the simple MOLB type geometry, Case 1, has the highest maximum temperature gradients in comparison the cases with the embedded porous pipe, as illustrated in fig. 5(b). It also shows higher average temperatures at lower current densities, as shown in fig. 5(a). For example, the simple MOLB type geometry at 5600 A/m² (power density of 3350 W/m²) has a maximum temperature gradient of 230 K, while for the same current density, Cases 2-4 reach a maximum temperature gradient of 90 K, 65 K, and 110 K, respectively. However, these decreases in the maximum temperature gradient directly affect the power density due to ohmic losses. The power densities for Cases 2-4 are around of 3150 W/m², 3100 W/m², and 3170 W/m², respectively, *i.e.* a reduction in power density of up to 8%, while the reduction in the maximum temperature gradient

Results and discussion

The voltage at different current densities for Cases 1-4 is compared in fig. 4. It can be seen that the behavior of the current density curves is similar for all cases, and the performance of the SOFC is the same for current densities below 2000 A/m². The maximum current density reached is around 5600 A/m² that corresponds to its power density of 3350 W/m² for the simple geometry, Case 1. This limit is due to the average temperature at which the SOFC can be operated (around 1273 K) as shown in fig. 5(a). For the geometries with

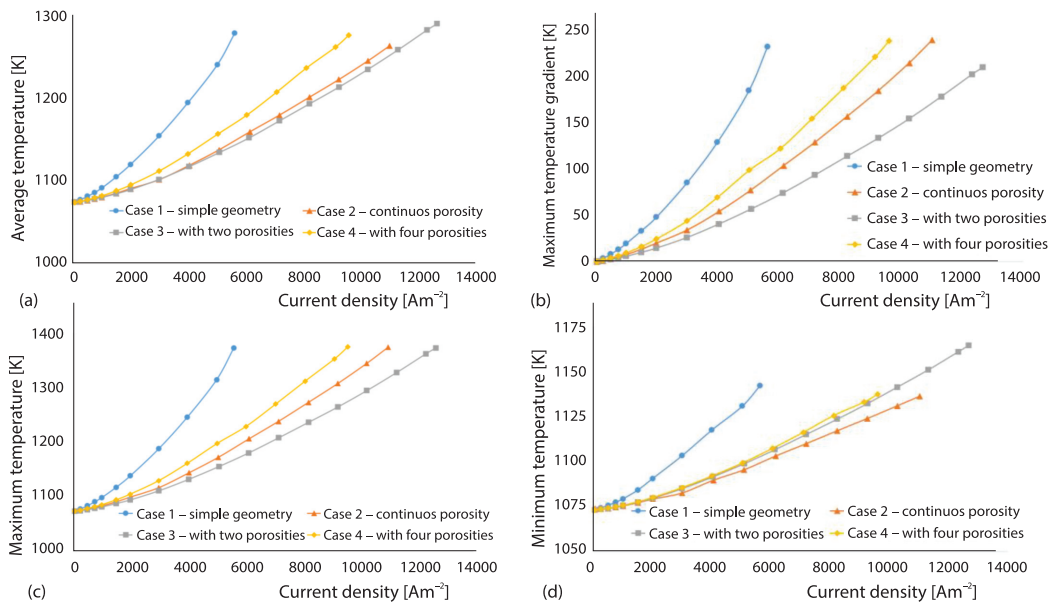


Figure 5. Curves of temperature vs. current density; (a) average temperature, (b) maximum temperature gradient, (c) maximum local temperature, and (d) minimum local temperature

is around 70%. Case 3 presented the lowest maximum temperature gradient at higher current densities, according to fig. 5(b), due to the maximum and the minimum local temperature at different current densities, figs. 5(c) and 5(d).

In fig. 6, it is shown a detailed comparison of the consumption and production of the species (H_2O , H_2 , and O_2) on the SOFC electrode-electrolyte interface varying the current

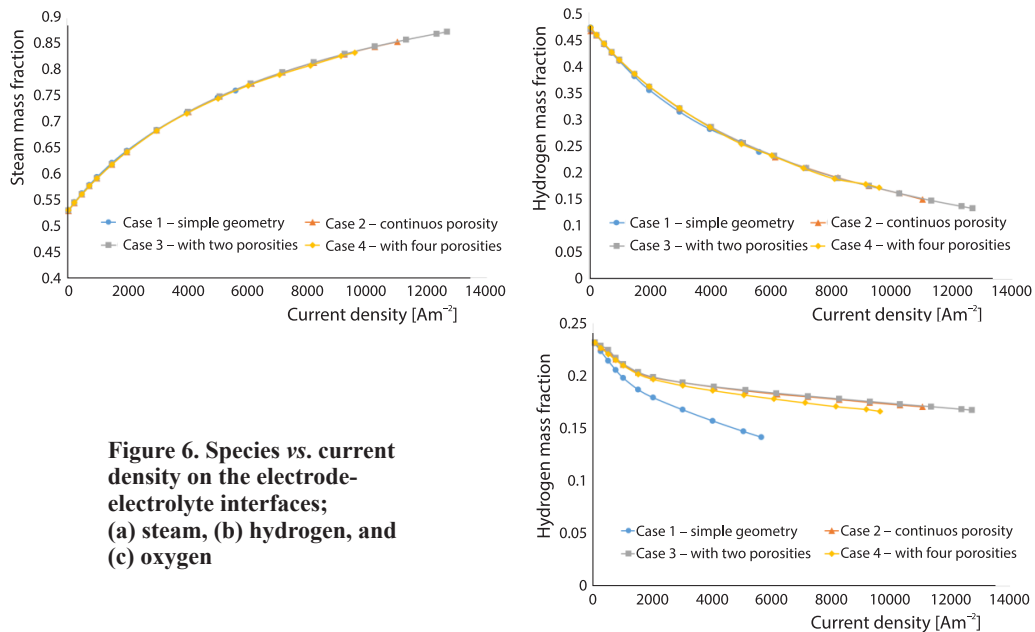


Figure 6. Species vs. current density on the electrode-electrolyte interfaces; (a) steam, (b) hydrogen, and (c) oxygen

density until the average temperature of 1273 K is reached. The production of steam and the H_2 consumption have the same behavior for all cases, as it can be observed in figs. 6(a) and 6(b). On the other hand, the O_2 consumption is different for each case, as shown in fig. 6(c). The simple geometry exhibits lower O_2 mass fractions than the other cases as the current density increases, due to the counter flow arrangement between the air channel and the porous pipe. The O_2 species provided for the flow in the air channel are consumed by the electrochemical reactions on the cathode-electrolyte interface and decreases in the air-flow channel direction as is illustrated in fig. 8(a) for the simple MOLB type geometry, the inclusion of the porous pipe diminishes the concentration losses because the O_2 species are replaced by the fluid provided in the porous pipe, fig. 8(b).

Detailed comparisons of the different physical phenomena inside the SOFC are shown in figs. 7-10 at a power density of 3350 W/m^2 , corresponding to the maximum current density of 5600 A/m^2 reached in Case 1, and the MOLB type geometries with the embedded porous pipe with a continuous porosity, Case 2, two porosities, Case 3, and four porosities, Case 4. The current density distributions in the electrode-electrolyte interface between the different cases are compared in fig. 7.

The figs. 7(a) and 7(b) illustrates the behavior of the current density for the case without the porous pipe and for all the cases considering the embedded porous pipe, respectively, which show same trend as in fig. 4 at different current densities. However, the value of the average current density on the interface electrode-electrolyte is around 10% higher (6100 A/m^2) for the cases with the embedded porous pipe to reach the power density of 3350 W/m^2 . This increment in the current density is due to the average temperature reduction, fig. 5, which increase the ohmic losses; consequently, the current density has to be increased to obtain the required power density. This behavior is due to the high temperature gradient reached inside of the fuel cell, as it is illustrated in fig. 10, in comparison the cases that consider the porous pipe.

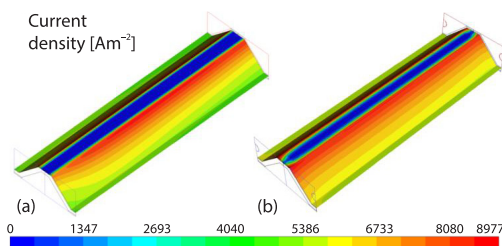


Figure 7. Current density distribution in the electrode-electrolyte interface at a power density of 3350 W/m^2 ; (a) Case 1 and (b) Cases 2-4

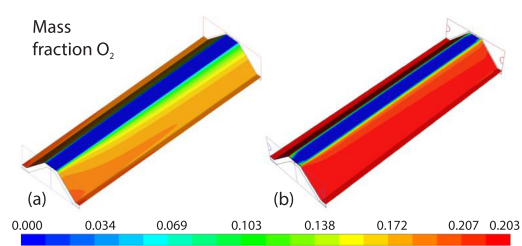


Figure 8. The O_2 mass fraction distribution in the cathode-electrolyte interface at a power density of 3350 W/m^2 ; (a) Case 1 and (b) Cases 2-4

At higher temperatures, the ohmic losses decrease and the current density increases. Consequently, the consumption of the O_2 species in the electrolyte-cathode interface is higher near to the exit of the air-flow in the simple geometry configuration, fig. 8(a). For the cases with the porous pipe, the concentration of O_2 species is higher (an increment of around 28% of the average O_2 mass fraction available on the cathode-electrolyte interface) and more homogeneous, fig. 8(b), due to the counter flow arrangement between the air channel and the porous pipe, meaning that the O_2 species, provided for the fluid-flow in the air channel that it is consumed by the electrochemical reactions along of the cathode interface, is replaced for the fluid-flow provided in the porous pipe. The similar current density distribution on the inter-

face electrode-electrolyte of the SOFC, in the cases with the porous pipe, fig. 7(b), is due to the similarity of O_2 , H_2 and temperature distributions at the anode and the cathode interfaces, as it should be noted in figs. 8-10.

The H_2 mass fraction distributions between the MOLB type geometry SOFC, Case 1, and the MOLB type geometry SOFC with a porous pipe embedded with a continuous porosity, Case 2, with two porosities, Case 3, and with four porosities, Case 4, are compared in fig. 9. The anode-electrolyte interfaces show similar H_2 mass fraction consumption for all cases due to the similar trends, as it can be seen in fig. 6(b). The upper surface has a higher H_2 mass fraction concentration, due to the lack of O_2 in the cathode-electrolyte interface to produce the current density, as illustrated in fig. 8. The H_2 mass fraction decreases along the fuel flow direction due to the electrochemical reactions that take place in the TPB.

The temperature distributions in the electrode-electrolyte interface for all cases are compared in fig. 10. As it was expected, the temperature increases along the fuel cell due to the heat generated by the exothermal reaction, ohmic losses and activation losses. A more homogeneous temperature distribution in Cases 2-4 can be observed. The maximum temperature gradient achieved for Case 1 is around 230 K (without the porous pipe), while the maximum temperature gradient achieved for Cases 2-4 are 103 K, 74 K, and 121 K, respectively, fig. 5(b). The lowest temperature gradient (74 K) corresponds to Case 3 with two different porosities along the porous pipe. The average temperatures achieved are: 1277 K for Case 1, 1158 K for Case 2, 1151 K for Case 3, and 1178 K for Case 4, fig. 5(a). In all the cases, the highest temperature occurs at the upper part of the fuel cell near to the fuel exit, due to the electrochemical reactions that take place in the TPB, fig. 10.

Conclusions

The local transport characteristics inside the SOFC, such as: electric fields, species concentration distributions, and the temperature distribution between the simple MOLB type geometry SOFC and the MOLB type geometry SOFC with embedded porous pipe considering constant and variable porosities are compared. After the comparison, the main conclusions are as follows.

- The performance of the SOFC is similar for current densities below 2000 A/m^2 for all the cases analyzed.

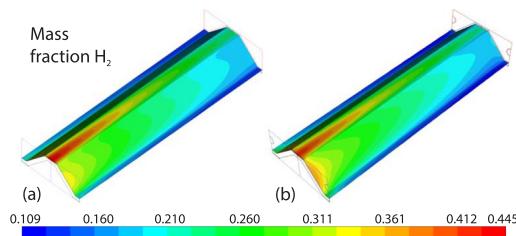


Figure 9. The H_2 mass fraction distributions in the anode-electrolyte interface at a power density of 3350 W/m^2 ; (a) Case 1 and (b) Case 2-4

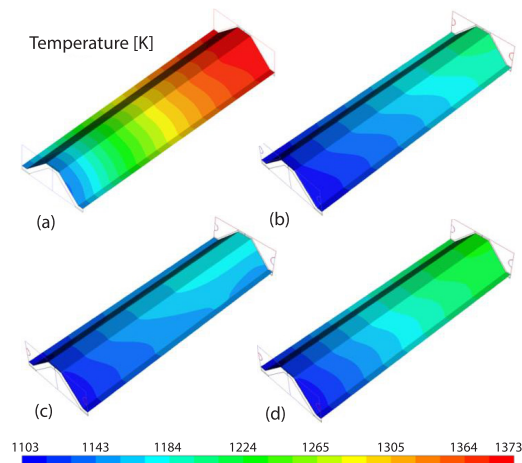


Figure 10. Temperature distribution in the electrode-electrolyte interface at a power density of 3350 W/m^2 ; (a) Case 1, (b) Case 2, (c) Case 3, and (d) Case 4

- The averaged current density in the case of the simple MOLB type geometry is limited due to the maximum temperature reached at 5600 A/m² while for the case with the embedded porous pipe with two sections an average current density of 12700 A/m² can be reached.
- The consumption of H₂ has the same behavior for all the current density tested, while the availability of the O₂ on the cathode-electrolyte interface is around 28% higher in the cases with the porous pipe in comparison with the simple MOLB type geometry, this provokes a decrease in the concentration losses of the SOFC.
- In general, a lower average temperature was obtained in all the cases that consider the embedded porous pipe in the MOLB type SOFC at the different current densities analyzed.
- Considering the cases with the embedded porous pipe, the temperature gradient is reduced by approximately 70%.
- The use of a porous pipe embedded in the air channel showed that it is possible to have a wider operating range of a MOLB type SOFC, and it allowed to obtain a more homogeneous temperature distribution on the electrode-electrolyte interface of the SOFC, consequently, there is the possibility of reducing the thermal stress in the SOFC.

Acknowledgment

The authors gratefully acknowledge to the National Council of Science and Technology (CONACYT), Mexico, for financial support under the *Proyecto Apoyado por el Fondo Sectorial de Investigacion para la Educacion*, I1200/169/2019 MOD.ORD./38/2019 FONDO SECTORIAL DE INVESTIGACIÓN PARA LA EDUCACION CB2017-2018 GENERAL A1-S-9539.

Nomenclature

D_{ij} – mass diffusion coefficient, [m²s⁻¹]
 $D_{i,\text{eff}}$ – effective mass diffusion coefficient, [m²s⁻¹]
 F – Faraday constant, [96487 Cmol⁻¹]
 h – enthalpy, [Jkg⁻¹]
 h_i – specific enthalpy of species i , [Jkg⁻¹]
 j – current density, [Am⁻²]
 j_0 – exchange current density, [Am⁻²]
 \vec{J}_i – diffusive flux of species i , [kgm⁻²s⁻¹]
 k_g – gas phase thermal conductivity, [Wm⁻¹K⁻¹]
 k_s – solid phase thermal conductivity, [Wm⁻¹K⁻¹]
 K – permeability of the porous media, [m²]
 k_{eff} – thermal effective conductivity, [Wm⁻¹K⁻¹]
 M_i – molecular weight of the species i , [kgmol⁻¹]
 n_e – number of electrons, [-]
 p – pressure, [Pa]
 R – universal gas constant, [Wmol⁻¹K⁻¹]
 S_c – energy source term, [Wm⁻³s⁻¹]
 S_i – species source term, [kgm⁻³s⁻¹]

T – emperature, [K]
 \vec{v} – vector velocity, [ms⁻¹]
 v – velocity, [ms⁻¹]
 V – voltage, [V]

Greek symbols

β – transfer coefficient
 ε – porosity, [-]
 η_{act} – activation potential, [V]
 η_{ohm} – ohmic loss, [V]
 η_{conc} – concentration loss, [V]
 μ – viscosity, [ms⁻²]
 ρ – density, [kgm⁻³]
 σ – electrical conductivity, [Ω⁻¹m⁻¹]
 τ – tortuosity, [-]
 ω_i – mass fraction of species i
 ϕ – electrical potential, [V]

References

- [1] Tushar, C., *et al.*, The CFD Modelling of SOFC Cogeneration System for Building Application, *Energy Procedia*, 109 (2017), 3, pp. 361-368
- [2] Sanjay, T. C., Thermodynamic Assessment of Advanced SOFC-Blade Cooled Gas Turbine Hybrid Cycle, *International Journal of Hydrogen Energy*, 42 (2017), 4, pp. 10248-263
- [3] Singh, A., Singh, O., Investigations on SOFC-HAT-sCO₂ Based Combined Power and Heating Cycle, *Materials Today: Proceedings*, 38 (2021), 1, pp. 122-128
- [4] Pitakthapanaphong, S., Busso, E. P., Finite Element Analysis of the Fracture Behaviour of Multi Layered Systems Used in Solid Oxide Fuel Cell Applications, *Model Simul. Mater. Sci. Eng.*, 13 (2005), 4, pp. 531-540

- [5] Bacigalupo, A., *et al.*, Effective Elastic Properties of Planar SOFC: A Non-Local Dynamic Homogenization Approach, *International Journal of Hydrogen Energy*, 39 (2014), 9, pp. 15017-15030
- [6] Dong, S. K., *et al.*, Design and Numerical Analysis of a Planar Anode-Supported SOFC Stack, *Renewable Energy*, 94 (2016), 8, pp. 637-650
- [7] Ghorbani, B., Vijayaraghavan, K., A Review Study on Software Based Modelling of Hydrogen-Fueled Solid Oxide Fuel Cells, *International Journal of Hydrogen Energy*, 44 (2019), 5, pp. 13700-13727
- [8] Kong, W., *et al.*, Residual Stress Analysis of a Micro-Tubular Solid Oxide Fuel Cell, *International Journal of Hydrogen Energy*, 41 (2016), 9, pp. 16173-16180
- [9] Tikiz, I., *et al.*, The CFD Modelling and Experimental Validation of Cell Performance in a 3-D Planar SOFC, *International Journal of Hydrogen Energy*, 44 (2019), 6, pp. 15441-15455
- [10] Park, J. G., *et al.*, The Current Density and Temperature Distributions of Anode-Supported Flat-Tube Solid Oxide Fuel Cells Affected by Various Channel Designs, *International Journal of Hydrogen Energy*, 36 (2011), 8, pp. 9936-9944
- [11] Park, J. G., Bae, J. M., Characterization of Electrochemical Reaction and Thermo Fluid Flow in Metal-Supported Solid Oxide Fuel Cell Stacks with Various Manifold Designs, *International Journal of Hydrogen Energy*, 37 (2012), 1, pp. 1717-1730
- [12] Shang, S., *et al.*, A Model for Oxidation-Induced Stress Analysis of Ni-Based Anode Supported Planar Solid Oxide Fuel Cell, *International Journal of Hydrogen Energy*, 44 (2019), 6, pp. 16956-16964
- [13] Hwang, J. J., *et al.*, Detailed Characteristic Comparison between Planar and MOLB-Type SOFC, *Journal of Power Sources*, 143 (2005), 4, pp. 75-83
- [14] Yang, Y., *et al.*, Comparison of Heat and Mass Transfer between Planar and MOLB-Type SOFC, *Journal of Power Sources*, 177 (2008), 3, pp. 426-433
- [15] Tinh, X. H., A 3-D Model for Transient Performance of a Solid Oxide Fuel Cell, *International Journal of Hydrogen Energy*, 39 (2014), 4, pp. 6680-6688
- [16] Amirpiran, A., *et al.*, Planar SOFC System Modelling and Simulation Including a 3-D Stack Module, *International Journal of Hydrogen Energy*, 41 (2016), 1, pp. 2919-2930
- [17] Chelmehsara, M. E., Javad, M., Techno-Economic Comparison of Anode-Supported, Cathode-Supported, and Electrolyte Supported SOFC, *International Journal of Hydrogen Energy*, 43 (2018), 8, pp. 15521-15530
- [18] Hwang, J. J., *et al.*, Computational Analysis of Species Transport and Electrochemical Characteristics of a MOLB-Type SOFC, *Journal of Power Sources*, 140 (2005), 10, pp. 235-242
- [19] Yunzhen, Y., *et al.*, Comparison of Heat and Mass Transfer between Planar and MOLB-Type SOFC, *Journal of Power Sources*, 177 (2008), 3, pp. 426-433
- [20] Ramirez-Minguela, J. J., *et al.*, Study of the Entropy Generation in a SOFC for Different Operating Conditions, *International Journal of Hydrogen Energy*, 41 (2016), 6, pp. 8978-8991
- [21] Ramirez-Minguela, J. J., *et al.*, Energy and Entropy Study of a SOFC Using Biogas from Different Sources Considering Internal Reforming of Methane, *International Journal of Heat and Mass Transfer*, 120 (2018), 1, pp. 1044-1054
- [22] Ramirez-Minguela, J. J., *et al.*, Entropy Generation Analysis of a Solid Oxide Fuel Cell by Computational Fluid Dynamics Influence of Electrochemical Model and Its Parameters, *Thermal Science*, 22 (2018), 1, pp. 577-578
- [23] Ramirez-Minguela, J. J., *et al.*, Internal Reforming of Methane in a Mono-Block-Layer Build Solid Oxide Fuel Cell with an Embedding Porous Pipe: Numerical Analysis, *Energy Conversion and Management*, 79 (2014), 3, pp. 461-469
- [24] Ramirez-Minguela, J. J., *et al.*, Solid Oxide Fuel Cell Numerical Study: Modified MOLB-Type and Simple Planar Geometries with Internal Reforming, *Electrochimica Acta*, 159 (2015), 3, pp. 149-157